

# Aviation Turbulence Induced by the Interaction between a Jet Stream and Deep Convection

Haoming Chen<sup>1</sup>, Xiaoming Shi<sup>2</sup>, Christy Yan-Yu Leung<sup>3</sup>, Ping Cheung<sup>3</sup>, and Pak Wai Chan<sup>3</sup>

<sup>1</sup>Hong Kong University of Science and Technology

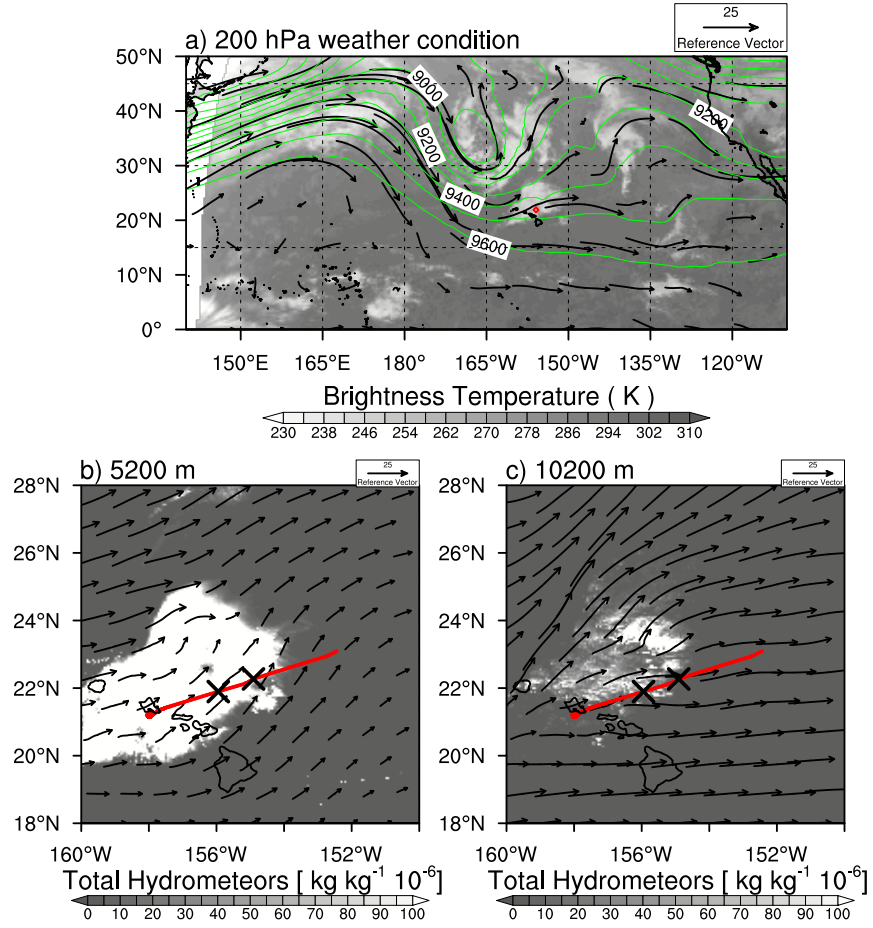
<sup>2</sup>Division of Environment and Sustainability, Hong Kong University of Science and Technology

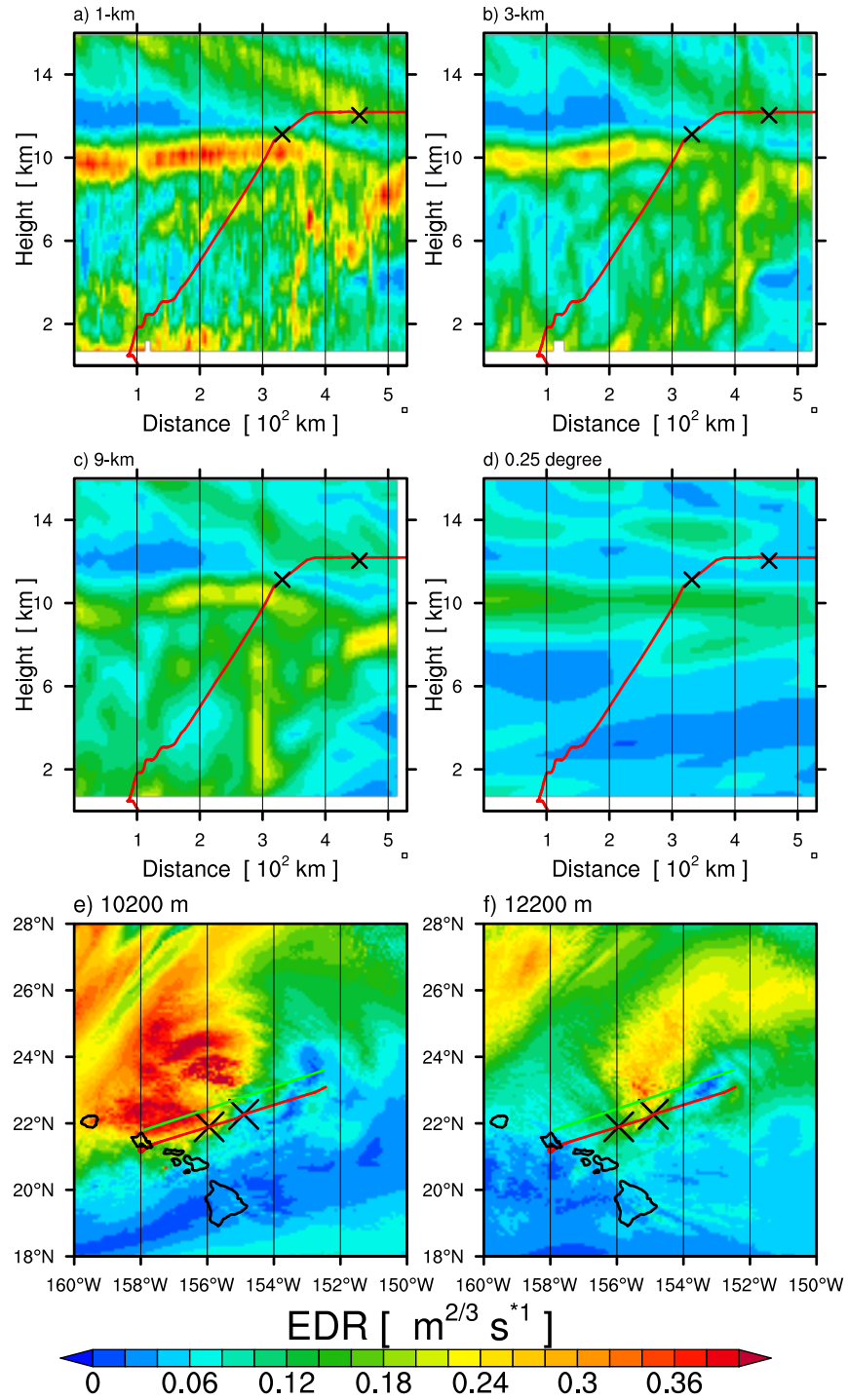
<sup>3</sup>Hong Kong Observatory

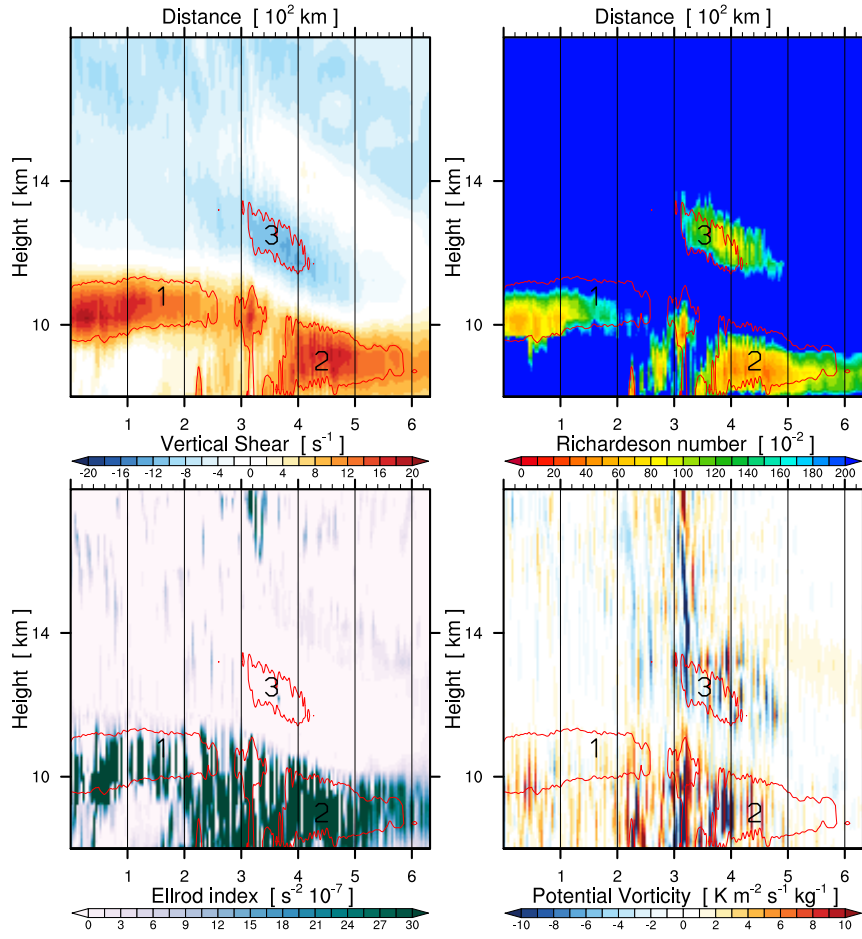
June 1, 2023

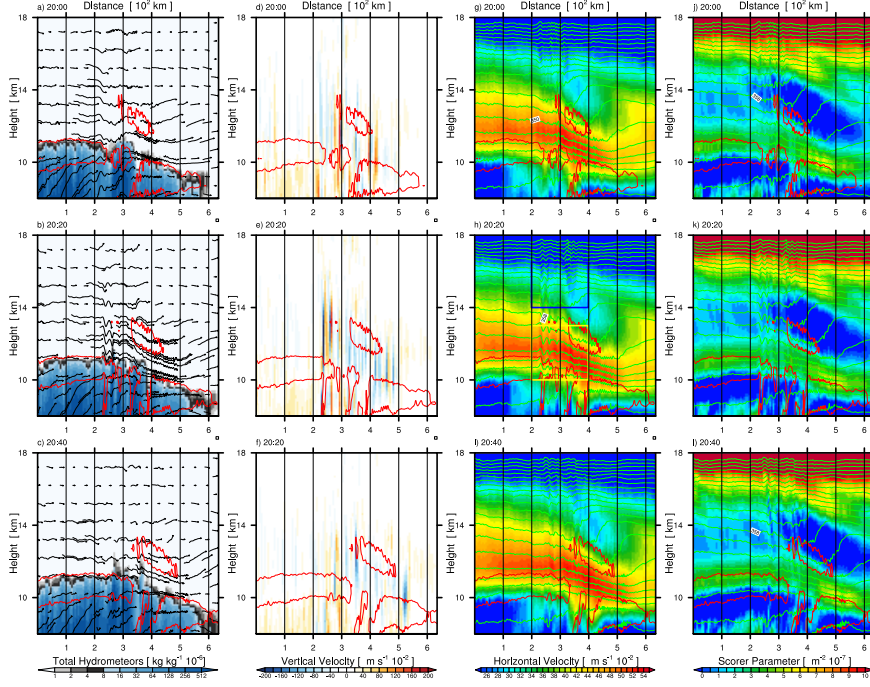
## Abstract

On December 18, 2022, Hawaiian Airlines flight HA35 encountered severe turbulence in a cloud-free region without warning. We simulated this incident using the Model for Prediction Across Scales (MPAS) with a convective permitting grid. We found that the turbulence formed due to the Kelvin-Helmholtz instability (KHI) generated by strong vertical wind shear. At low altitudes, deep convection caused a decrease in wind speed in both upstream and downstream regions. At upper levels, the jet descended and accelerated after flowing over the convection, which acted like a barrier and produced a situation similar to a downslope windstorm. The low Scorer parameter above the jet and the self-induced critical level created the locally enhanced descending jet stream, which destabilized the flow through KHI.









1  
2  
3  
4  
5  
6  
7  
8  
9  
10  
11  
12  
13  
14

# Aviation Turbulence Induced by the Interaction between a Jet Stream and Deep Convection

Haoming Chen<sup>1</sup>, Xiaoming Shi<sup>1</sup>, Christy Yan Yu Leung<sup>2</sup>, Ping Cheung<sup>2</sup>, Pak  
Wai Chan<sup>2</sup>

<sup>1</sup>Division of Environment and Sustainability, Hong Kong University of Science and Technology, Hong  
Kong, China  
<sup>2</sup>Hong Kong Observatory, Hong Kong, China

## Key Points:

- A regionally convection-permitting model and a new eddy dissipation rate calculation method were used to predict aviation turbulence.
- Deep convection acted like terrain and interacted with a jet stream, causing an upper-level windstorm downstream of the convection top.
- Severe turbulence upstream and downstream of convection was due to different mechanisms, but both related to Kelvin-Helmholtz instability.

## Abstract

On December 18, 2022, Hawaiian Airlines flight HA35 encountered severe turbulence in a cloud-free region without warning. We simulated this incident using the Model for Prediction Across Scales (MPAS) with a convective permitting grid. We found that the turbulence formed due to the Kelvin-Helmholtz instability (KHI) generated by strong vertical wind shear. At low altitudes, deep convection caused a decrease in wind speed in both upstream and downstream regions. At upper levels, the jet descended and accelerated after flowing over the convection, which acted like a barrier and produced a situation similar to a downslope windstorm. The low Scorer parameter above the jet and the self-induced critical level created the locally enhanced descending jet stream, which destabilized the flow through KHI.

## Plain Language Summary

On December 18, 2022, Hawaiian Airlines flight HA35 encountered severe turbulence without warning, resulting in injuries to some passengers and damage to the equipment. This unusual incident requires careful investigation to broaden our understanding of aviation turbulence. A numerical model at kilometer-scale resolution was used to simulate this case and reveal the dynamics, and we successfully captured the occurrence of turbulence with the simulation. The cause of the turbulence was a previously unknown mechanism. It involves the interaction between the deep convection that acted as a barrier and an upper-level jet. Severe turbulence was generated in a situation similar to a downslope windstorm near the ground due to mountains. This interaction caused turbulence in different locations near the strong convection, making the turbulence unpredictable because it occurs in cloud-free regions and cannot be detected by airborne radar.

## 1 Introduction

The turbulence in aviation is a significant contributor to weather-related incidents, causing injuries, occasional fatalities, and structural damage annually. Furthermore, it incurs considerable operational expenses for airlines, resulting in schedule disruptions and air traffic management challenges, amounting to millions of dollars (Tvaryanas, 2003; R. D. Sharman, Doyle, & Shapiro, 2012; Kim & Chun, 2016; R. Sharman & Lane, 2016a). Aviation turbulence is classified according to its sources: convection-induced turbulence (CIT), mountain wave turbulence (MWT), and clear-air turbulence, which are always generated by atmospheric instabilities, such as static, Kelvin–Helmholtz (KHI), convectively, conditional instabilities (R. Sharman & Lane, 2016b). Specifically, turbulence motions can be active in convection and its surrounding air because of moist instability. They can be generated by the strong deformation of the flow near the cloud and gravity wave breaking (Lane et al., 2003; Trier et al., 2012).

Topography can also induce turbulence because of the formation of gravity waves over the lee side of the mountain when flow passes the terrain. The significant amplitude and fragmentation of these waves induce turbulence. This phenomenon depends on the characteristics of the upstream environment, terrain geometry, and atmospheric stability at different altitudes (Clark & Peltier, 1984; R. Sharman & Lane, 2016b). At high altitudes, the “critical layers” where the wind reverses direction with height are important (R. D. Sharman, Trier, et al., 2012); at low altitudes, the possible “hydraulic jump” can make the flow turbulent (Prósper et al., 2019). Hydraulic jump derives from hydraulics and is a phenomenon that the thickness of a flow is rapidly increased. It usually occurs when a high-velocity fluid enters a low-velocity region, where the thickness of the fluid rises due to the opposite relationship between the thickness and energy of the supercritical and subcritical flow. Previous researchers have primarily examined the effects of MWT at high altitudes, as it is the altitude range that directly impacts aircraft.

64 However, what will happen if this terrain is suspended in the air? Fujita (1982) found  
65 that deep convection can act like a topographical feature (virtual terrain), inducing the  
66 upstream flow to either deflect or go over it. Under appropriate atmospheric conditions  
67 and convection, it can even generate a hydraulic jump at high altitudes, resulting in tur-  
68 bulance downwind (O’Neill et al., 2021). Our research reveals that strong convection func-  
69 tions as a topographical feature, inducing high-altitude jet streams to generate turbu-  
70 lence in distinct regions downstream of the convection. This mechanism differs from pre-  
71 vious studies focused on CIT though this region has strong convection. Furthermore, the  
72 velocity of the jet increase as they descend, leading us to believe that this process is sim-  
73 ilar to the formation mechanism of a downslope windstorm.

74 Downslope windstorms have been observed in mountainous regions worldwide (Fudeyasu  
75 et al., 2008; Koletsis et al., 2009) and relevant studies utilized various methodologies such  
76 as observation and numerical simulations (Doyle & Smith, 2003; Klemp & Lilly, 1975),  
77 which showed the nonlinear effects on large-amplitude mountain waves. To explain these  
78 nonlinear effects, various theories have been developed: 1) the flow undergoes a transi-  
79 tion from subcritical flow upstream to supercritical flow downstream (D. R. Durran, 1986;  
80 Smith, 1985; Long, 1953); 2) the upward propagating waves are reflected downward by  
81 an area where the Scorer parameter changes rapidly, which creates a superposition of  
82 the wave to increase the wind velocity (Klemp & Lilly, 1975); and 3) the “self-induced  
83 critical layer” can trap the energy to increase the wave amplitude (Peltier & Clark, 1979;  
84 Clark & Peltier, 1984).

85 In this research, we used the Model for Prediction Across Scales (MPAS) to study  
86 a case of severe aviation turbulence that happened near the Hawaiian Islands. The ac-  
87 cident left 25 people injured, some seriously, and the condition of “smooth with clear skies”  
88 (Oxenden, 2023) suggests its complex mechanisms involved. MPAS has the flexibility  
89 and advantage to cover global circulation but refine its grid mesh to a convection-permitting  
90 resolution regionally. It is found that the severe turbulence is caused by a new mecha-  
91 nism not considered before in aviation turbulence, which is due to the interaction be-  
92 tween the jet stream and deep convection.

## 93 2 Models and Methods

### 94 2.1 MPAS Setup

95 The MPAS version 7 is used in this study for regionally convection-permitting sim-  
96 ulations. It is characterized by a non-hydrostatic dynamical core using unstructured Voronoi  
97 meshes and C-grid discretization (Skamarock et al., 2012). The global variable-resolution  
98 mesh can have finer resolutions in interested areas. This study focuses on aviation tur-  
99 bulance near Hawaii Islands. Our experiments are designed with 1 ~ 60, 3 ~ 60 and  
100 9 ~ 60 km meshes. Figure S1 in supplementary materials shows the mesh configura-  
101 tions, which have higher resolution near the Hawaiian Islands and offshore waters and  
102 gradually change to 60-km resolution in the background. The analysis is the results from  
103 the 1 ~ 60 mesh if not specified otherwise. Different resolutions help to test the sen-  
104 sitivity of the simulated convection and turbulence to grid spacings.

105 The initial conditions are based on the European Centre for Medium-Range Weather  
106 Forecast (ECMWF) fifth-generation reanalysis (ERA5) data at a 0.25° horizontal grid  
107 spacing and 37 vertical levels (Bell et al., 2021). The initialization time of our simula-  
108 tions is approximately 6 hours before the occurrence of the incident. The MPAS has a  
109 vertical profile consisting of 55 layers, with the highest layer situated at an altitude of  
110 22 km above the surface. The experiments turned off the convection parameterization  
111 since switching it off can usually provide a higher intensity of turbulence. We used the  
112 MPAS microphysics suite, which uses the Thompson scheme (Thompson et al., 2008)  
113 for grid cells smaller than 10 km and the WSM6 scheme (Hong et al., 2006) for other cells,

114 the planetary boundary layer scheme suite, which uses the YSU (Hong, 2010) at the courser  
 115 resolution and the MYNN (Nakanishi & Niino, 2009) at the finer resolution. The Noah  
 116 land surface scheme (F. Chen & Dudhia, 2001), and the RRTMG short and longwave  
 117 radiation schemes (Mlawer et al., 1997; Iacono et al., 2000) are used in all simulations.

## 118 2.2 Calculation of Eddy Dissipation Rate (EDR)

119 A new method to estimate EDR based on convection-permitting model output and  
 120 subfilter-scale reconstruction has been developed by H. Chen et al. (2023). It has been  
 121 proven to be more effective in capturing turbulence than other methods. This method  
 122 separates subfilter scales into resolvable subfilter scales (RSFS) and subgrid scales (SGS).  
 123 The RSFS components have much more energy than the SGS component. Thus, we com-  
 124 pute the RSFS part only. Following (Chow et al., 2005). The reconstructed RSFS ve-  
 125 locity

$$\tilde{u}_i^* = \overline{\tilde{u}_i} + (I - G)\overline{\tilde{u}_i} + (I - G)(I - G)\overline{\tilde{u}_i} + \dots \quad (1)$$

126 where the overline denotes the filter, the tilde denotes discretization,  $\overline{\tilde{u}_i}$  is, therefore, the  
 127 grid variable from MPAS,  $I$  is the identity operator, and  $G$  is the filter. In this study,  
 128 the filter is a top-hat filter applied to all three dimensions. Keeping  $\overline{\tilde{u}_i}$  is the zero-order  
 129 reconstruction and is what we adopted. Including more terms on the right side of Eq. 1  
 130 generates higher-order reconstruction, which is not used in this study because it may oc-  
 131 casionally generate negative TKE.

132 After obtaining RSFS velocities, the RSFS TKE is

$$\text{TKE} = \frac{1}{2} \left( \overline{\tilde{u}_i^* \tilde{u}_i^*} - \overline{\tilde{u}_i^*} \overline{\tilde{u}_i^*} \right) \quad (2)$$

133 And assuming the turbulence is in the inertial subrange, the EDR is the following (Schumann,  
 134 1991),

$$\varepsilon^{1/3} = \left( \text{TKE}^{3/2} / L \right)^{1/3} \quad (3)$$

135 where  $L = (\lambda \Delta x \Delta y \Delta z)^{1/3}$  is the integral scale of the turbulence,  $\Delta x$ ,  $\Delta y$  and  $\Delta z$  are  
 136 grid spacings. In our calculations, we interpolated MPAS data from the unstructured  
 137 grid to  $0.008^\circ \times 0.008^\circ$  latitude-longitude grid before using the above equations. There-  
 138 fore,  $\Delta x$  and  $\Delta y$  are approximately 0.8 km for the region near Hawaii Islands.  $\Delta z$  is 500 m.  
 139  $\lambda = 8$  for our calculation. However, in principle, one could adjust this factor  $\lambda$  to cal-  
 140 ibrate EDR estimation for the operational forecast.

## 141 2.3 Other Physical Quantities

142 The Froude number (Fr) in this case was calculated from

$$\text{Fr} = \frac{U}{NH} \quad (4)$$

144 here, the  $U$  is the velocity of the upstream wind,  $N$  is the Brunt–Vaisala frequency, and  
 145  $H$  is the height of flow descent (O’Neill et al., 2021), and we extracted the flow by some  
 146 specific isentropes, it will be described later, so the  $U$  and  $N$  is the average in the flow.  
 147 If  $\text{Fr} \gg 1$ , the flow passes over the barrier with small changes (Carruthers & Hunt, 1990),  
 148 if  $\text{Fr} \ll 1$ , the flow will be blocked and have substantial nonlinear effects (Smolarkiewicz  
 149 & Rotunno, 1989), and the  $\text{Fr} \sim 1$  means transitional flow may happen.

150 The Scorer parameter  $l^2$ , an value to evaluate if a gravity wave can propagate through  
 151 a region, is defined as follows:

$$l^2 = \frac{N^2}{U^2} - \frac{1}{U} \frac{d^2 U}{dz^2} \quad (5)$$

152 Waves with horizontal wave numbers larger than  $l^2$  are evanescent (D. Durran, 2003).

### 3 Results

#### 3.1 Environmental Conditions

Figure 1 a) shows a map of the large-scale wind field, geopotential height and the brightness temperature from GOES-17(?, ?) at 200 hPa on December 18, 2022, 20:10 UTC. It exhibits extensive cloud coverage over the western Hawaiian Islands and over the sea to the northeast. The clouds are located in the exit region of a distorted mid-latitude jet stream, due to a low pressure in the northwest of Hawaii. Notably, the clouds' altitude is relatively low, and the airplane was traversing a cloud-free region. The wind near Hawaii is southwesterly, opposite to the direction of the aircraft's flight path.

The horizontal distributions of the total hydrometeors at altitudes of 5200 m and 10200 m are presented in Figure 1 b) and c), showing the consistency with observation, wherein the aircraft track is represented by a red line. The airplane's trajectory was located in a region with less convection around its path, but it was still affected by strong turbulence. Notably, the lower altitudes exhibit more convective activity, and some alerts about thunderstorms in the vicinity were raised. At high altitudes, convection is reduced, with sporadic strong convection forming a loosely organized arc perpendicular to the prevailing wind direction.

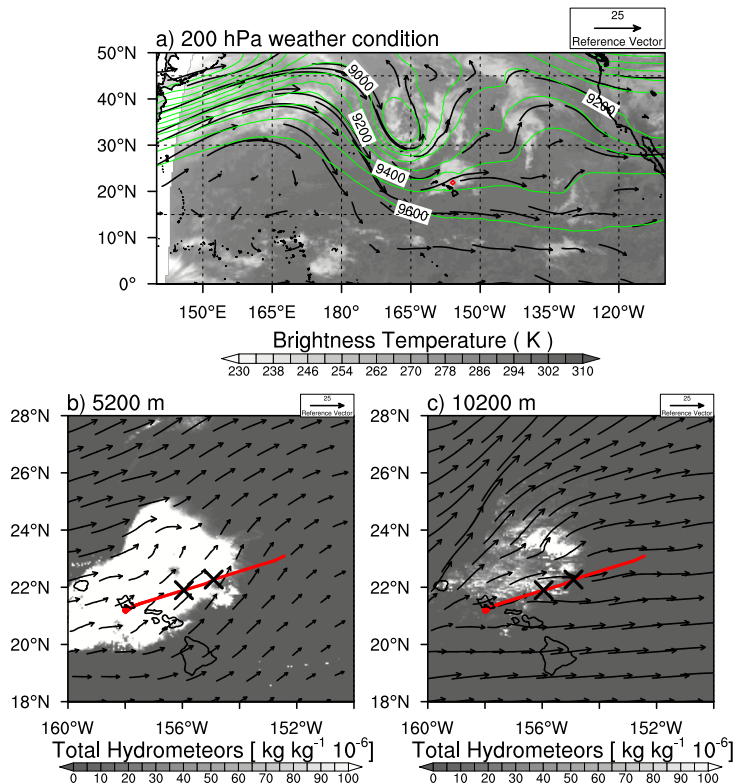


**Figure 1.** a) Horizontal distribution of brightness temperature (shading) from GOES-17, 200-hPa wind (vectors), and geopotential height (unit: m, green contour). b) total hydrometeors in MPAS simulation at 5200 m, c) as as (b) but at 10200 m. These data are on December 18, 2022, at 20:10 UTC. The red square in (a) indicates the location of aviation turbulence events. The red lines in (b) and (c) represent the airplane's path. The two crosses mark the positions of turbulence events

170 Additional figures about wind at different altitudes can be found in Figure S2 in  
 171 the supplementary material. It can be found that there exists a low-speed region to the  
 172 northwest of the airplane path, southwest of the convection, and the positions of con-  
 173 vection can be indicated in Supplementary Figure S3 with vertical velocity. This sug-  
 174 gests the influence of the convection system on the wind field, as evidenced by an increase  
 175 in speed over the convection.

### 176 3.2 Validation of Simulations

177 Based on media coverage and flight data, we know there were two approximate lo-  
 178 cations where the turbulence happened. Figure 2 shows the distribution of EDR on the  
 179 cross-section along the airplane’s trajectory from different simulations at 20:10 UTC on  
 180 December 18, 2022. The red line represents the aircraft’s path, while the two markers  
 181 denote the locations where turbulence incidents occurred. The lower marker, situated  
 182 at an altitude of 11 km, corresponds to the trajectory at 20:16 UTC. The higher marker,  
 183 positioned at an altitude of 12.5 km, corresponds to the trajectory at 20:08 UTC. In the  
 184 aircraft’s trajectory record, a rapid 500 ft descent was observed near this upper-level in-  
 185 cident, followed by a return to the original altitude.

186 In Figure 2, the  $x$ -coordinate denotes distance. The moderate and severe intensity  
 187 turbulence ( $\text{EDR} \geq 0.22$ ) has a descending distribution at altitudes exceeding 12 km,  
 188 with the wake just intersecting the flight track. At the altitude of 10 km, the turbulence  
 189 displays a stable, mostly horizontal distribution, with a thickness of approximately 1 km  
 190 within the  $x$ -range of 0 to 450 km, beyond which the altitude of the turbulent layer de-  
 191 creases to 8 ~ 10 km. Notably, the turbulence occupies a high altitude but is confined  
 192 to a narrow horizontal distance around  $x = 350$  km. There was a series of deep con-  
 193 vective systems in that area, serving as the source of this turbulence. Overall, the pat-  
 194 tern of turbulence remains qualitatively consistent at different resolutions. Similar dis-  
 195 tributions can be seen in ERA5 data, but there are some location discrepancies, and the  
 196 deep convection is missing. In two turbulence incident locations, all three MPAS sim-  
 197 ulations show EDR values significantly higher in surrounding regions. The higher res-  
 198 olution produced higher values. These resolution-depending results are consistent with  
 199 our previous resolution testing results and previous research(Barber et al., 2018).

200 Notably, the resolution dependency cannot be fixed by a simple adjustment with  
 201 a constant scaling factor. For example, if the 9-km resolution results are doubled to reach  
 202 the magnitude of 1-km resolution simulation results, it will overestimate the turbulence  
 203 in 6 ~10 km height range,  $x$  coordinate 100 ~ 300 km. Additionally, when observing  
 204 the coordinates of convective clusters, which are areas where turbulence appears in a col-  
 205 umn shape, the 1-km resolution results are further to the east, indicating a delay in the  
 206 development of convection in the low-resolution results. Therefore, the higher resolution  
 207 appears to be necessary for simulations.

208 Figure 2 e), f) shows the distributions of the EDR in different altitudes at 20:10  
 209 UTC on December 18, 2022, from the 1-km resolution simulation. The southern red lines  
 210 represent the flight path of the airplane. We found that, especially at high altitudes, the  
 211 eastern incident location is actually part of a large turbulence area. The wind speed map  
 212 (Fig. 1) also shows a low wind speed area to the northwest of the aircraft’s path, followed  
 213 by wind vectors pointing to a large area with intense turbulence. Therefore, in order to  
 214 better reveal the mechanism of turbulence, we can examine the section along the green  
 215 line, which is to the north of the flight trajectory.

### 216 3.3 Turbulence Generation Mechanisms

217 Figure 3 shows the cross-section (green line in Fig. 2) for different turbulence in-  
 218 dices overlaid by EDR contours for regions with EDR higher than 0.25. We marked three

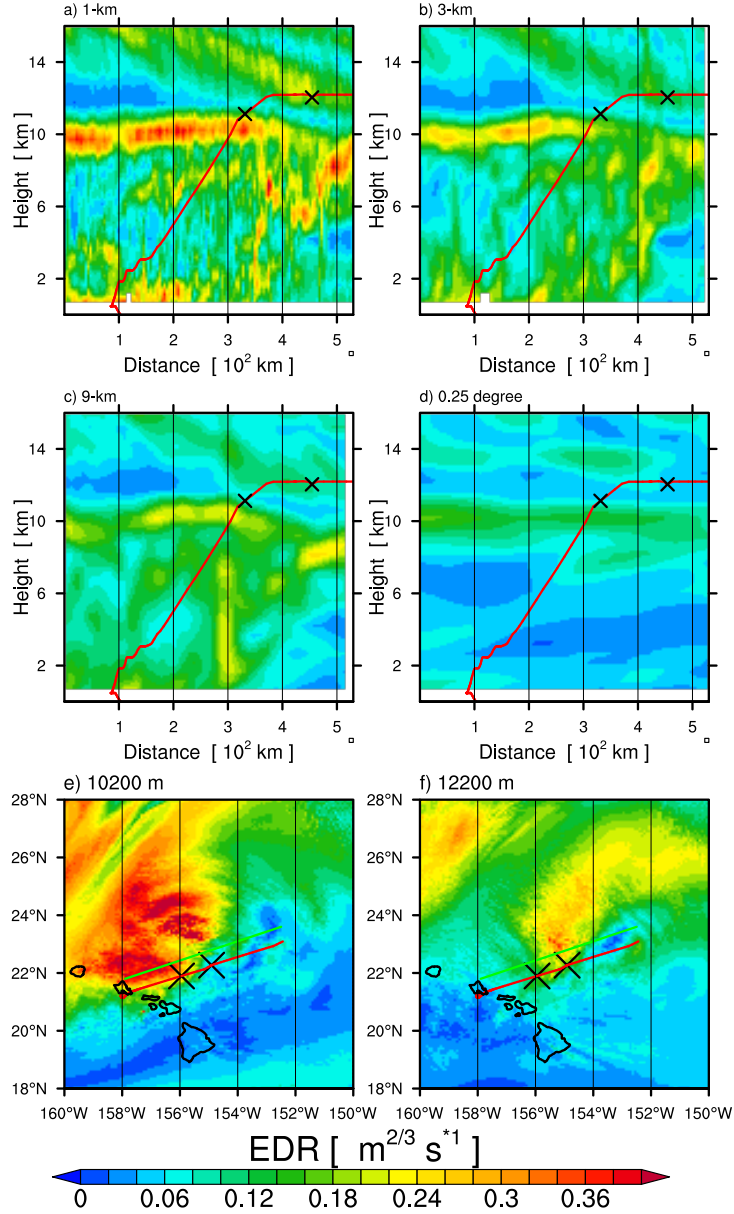


**Figure 2.** Cross sections along the path of the airplane, with the distribution of EDR from different resolutions a) 1 km, b) 3 km, c) 9 km and d) 0.25° and horizontal distribution of the EDR from 1- km mesh with different altitudes. e) 10200 m, f) 12200 m. at December 18, 2022, 20:10 UTC, while the ERA5 result is on December 18, 2022, 20:00 UTC. The red line represents the path of the airplane, the two notations represent the positions of turbulence events. The green line represents the new section.

219 regions, with each part exhibiting moderate or high-intensity turbulence. The first two  
 220 regions encompass the areas below the jet and on both the upstream and downstream  
 221 sides of the convection, respectively. The third section pertains to the region above the  
 222 descending jet.

223 By comparing the indices for turbulence based on wind shear and other different  
 224 mechanisms, we found that all turbulence in the three marked regions appears to be gen-  
 225 erated by the KHI, which is mainly driven by strong vertical wind shear. From Figure  
 226 3 a) and b), strong vertical wind shear, low Richardson number, and high EDR regions  
 227 tend to overlap. In Figure 3 c), the Ellrod index is greater than 25 over many areas, which  
 228 would be considered as severe turbulence (Ellrod & Knapp, 1992), but Region 3 is not  
 229 covered at all. In Figure 3 d), the regions where sign changes of potential vorticity (PV)  
 230 exist are considered to have turbulence (Audrey et al., 2011). The PV sign changes mainly  
 231 occur in the vicinity of convection, and this PV-based prediction is very inaccurate re-  
 232 garding the location of turbulence.

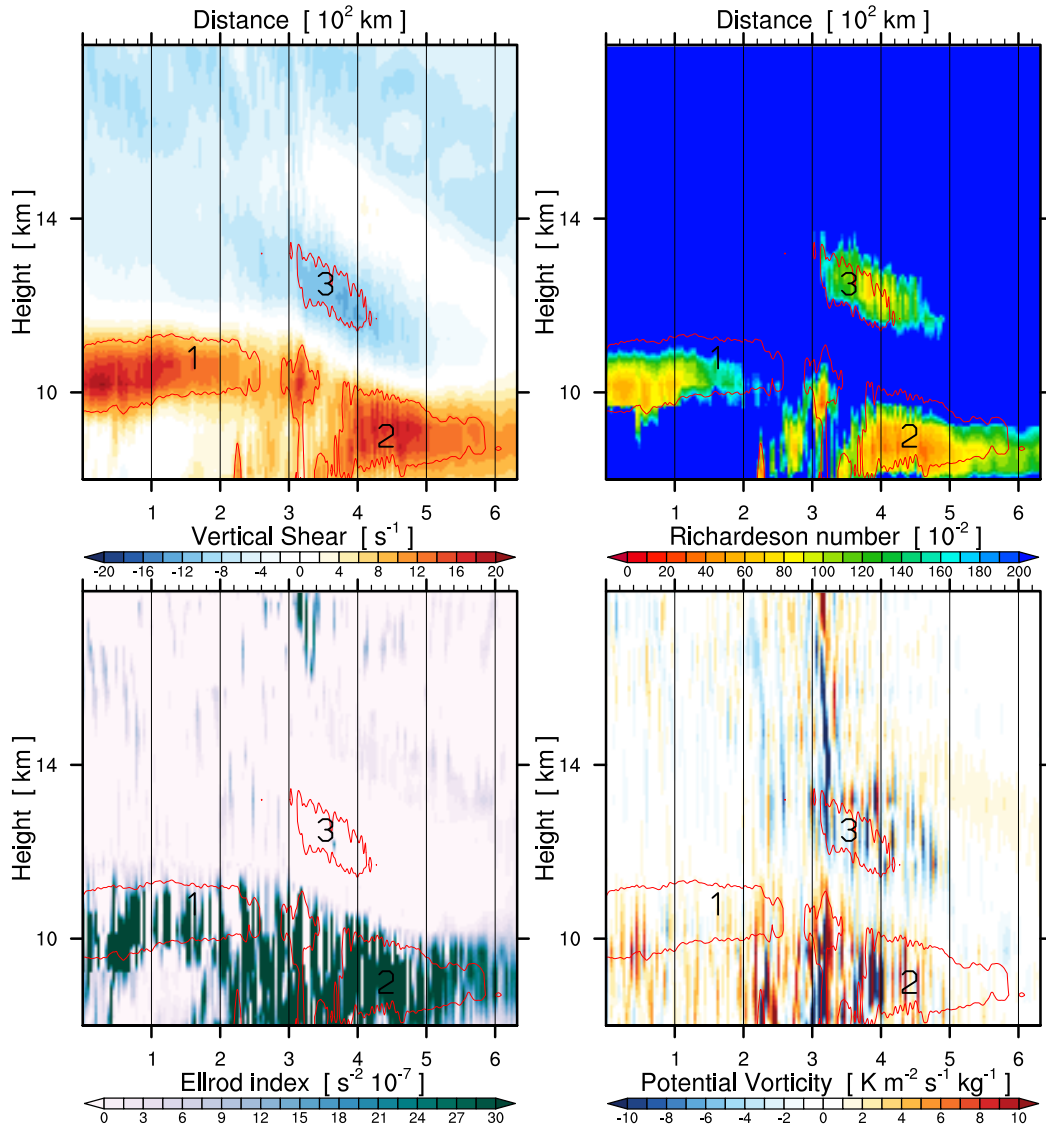


**Figure 3.** Vertical cross-sections of a) wind shear, b) Richardson number, c) Ellrod index, and d) potential vorticity on December 18, 2022, at 20:10 UTC. The area where EDR is higher than 0.25 is highlighted with the red contour in all panels. The numbers in the figure mark different turbulent regions.

233 In Regions 1 and 2. The hindering effect of convection caused low-speed areas up-  
 234 stream and downstream and combined with the jet at 11 km altitude, resulting in stronger  
 235 wind shear below the jet, leading to KHI.

236 The Region 3 appears to be unique because of the relatively low-speed air. It oc-  
 237 curs above the jet descent region, which results from the interaction between deep con-  
 238 vection and the preexisting jet. The turbulence in this region originates from a situa-  
 239 tion similar to a low-level downslope windstorm due to mountains. We will discuss the  
 240 details of the flow structure and mechanisms in the next section.

### 241 3.4 Windstorm Over Deep Convection

242 This section concentrates on how the high-altitude jet and convection interact to  
 243 yield flow acceleration when the jet flows over the convection, as well as the structure  
 244 of this ‘downslope’ jet.

245 Figure 4 shows cross-sections of simulated potential temperature, wind, vertical mo-  
 246 tions, and the Scorer parameter at 20:00, 20:20, and 20:40 UTC on December 18, 2022.  
 247 This figure reveals the location of the convection through the presence of strong verti-  
 248 cal velocity, which exhibits slow movement. The height of hydrometeors drops signifi-  
 249 cantly after crossing the strong convection. Concurrently, the altitude where the jet ac-  
 250 celeration occurs, as well as the turbulent region, follow the development and movement  
 251 of the convective system with time. Notably, at 20:20, the convective activity intensi-  
 252 fies at  $x$  coordinate of 240 km, causing the isentropes above to be warped upwards. These  
 253 flow characteristics suggest that the strong convection acted as a barrier to the jet stream.

254 Figure 4 indicates that below the altitude of 11 km and before reaching the  $x$ -coordinate  
 255 of 250 km, the wind vector exhibits an upward lift. There is a large positive area of ver-  
 256 tical velocities, which signifies the occurrence of an upward process of the flow to the west-  
 257 ern region of the convection and shows the topography-like effects from deep convection.  
 258 Meanwhile, the jet maintains a relatively stable height. Upon flowing over the convec-  
 259 tive system, the isentropes with a height between 10 ~ 14 km undergo a significant drop  
 260 in height, decreasing by 1.5 km in height within a horizontal range of approximately 180 km.  
 261 Moreover, the wind speed undergoes a notable increase during the descent at the down-  
 262 stream side of the convection, with the average wind speed rising from 40 to 50 m/s, in-  
 263 dicating the presence of a downslope storm-like high-speed region. At half of the descent  
 264 height, the isentropes adopt a wavy pattern with a short wavelength of approximately  
 265  $7 \sim 8$  km.

266 Some theories used to explain downslope windstorms require a critical layer. In res-  
 267 onant amplification theory, it is typically thought to isolate the effect of gravity waves  
 268 that propagate vertically, which may be induced by a directional shift in wind or strong  
 269 vertical shear. An area of a lower Scorer parameter or the lower Richardson number can  
 270 also lead to this effect. In the theory of transitional flow, since the Fr needs to be cal-  
 271 culated based on Equation 4, the obstacle’s height is important.

272 In our investigation, the high-altitude jet is a component of large-scale circulation  
 273 and is not ubiquitous across the entirety of high-altitude regions in middle latitudes. Con-  
 274 sequently, the vertical wind shear is substantial in the layers immediately above and be-  
 275 low the jet, as evidenced by Figure 4 j), k) and l). Additionally, a lower Scorer param-  
 276 eter is present at an altitude range of 12 ~ 14 km and 8.5 ~ 10 km prior to crossing  
 277 the convection.

278 Therefore, a well-functioning waveguide has been generated before traversing the  
 279 convection. Upon crossing the convection, the gravity waves are stimulated and reflected  
 280 back towards the jet from the low Scorer parameter region. It results in an increase in  
 281 the velocity of the jet due to the resonance as well as the wind shear, which leads to a

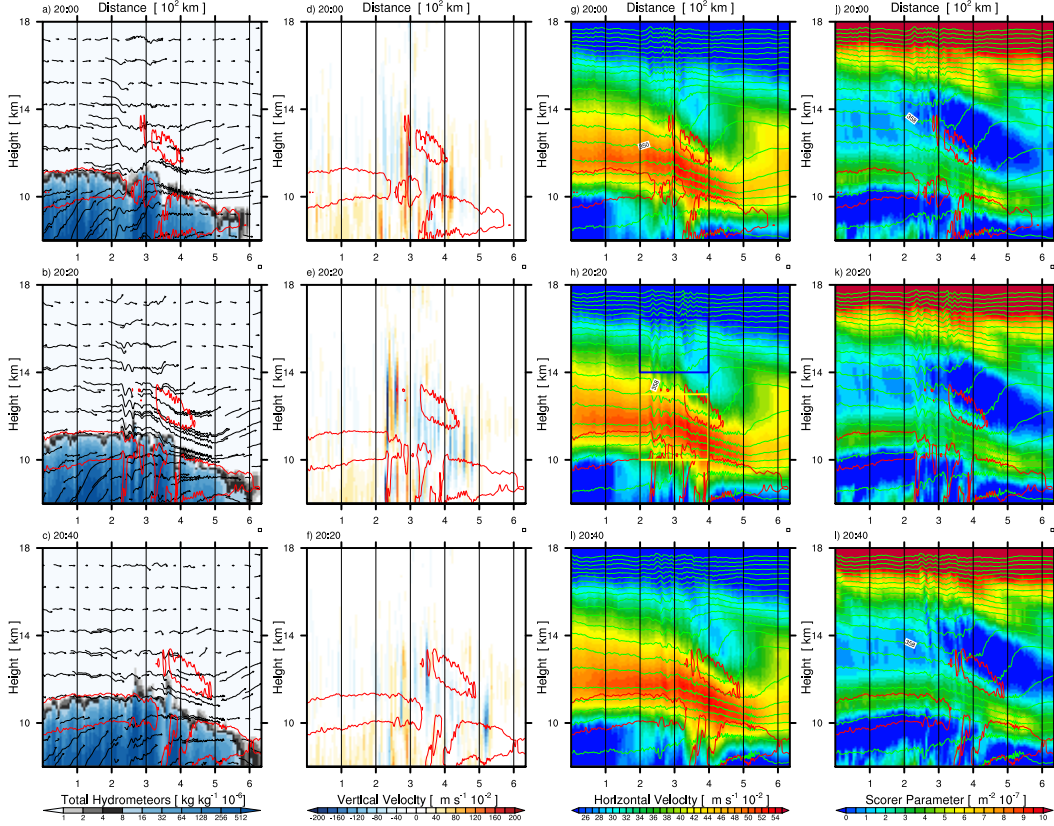


**Figure 4.** Cross-sections of different variables (columns). The rows represent different times on December 18, 2022, at 20:00, 20:20, and 20:40 UTC. a), b) and c) show total hydrometeors; d), e) and f) show the vertical velocity, g), h) and i) are the horizontal wind speed along the section; and j), k) and l) are the Scorer parameter. Wind vectors reference the orientation of the cross-section and are superimposed on a), b), and c). Potential temperature is superimposed as green contours with an interval of 4 K. The area where EDR is higher than 0.25 is highlighted with the red contour in all panels. shades)

282 lower scorer parameter at the higher altitude of the jet so that the wave can break here  
 283 more easily; it can be recognized as the self-induced critical level. Thus, a positive feed-  
 284 back system is established. In Figure 4 g), h) and i), there is an area of low-speed wind  
 285 between altitude 12.5 ~ 14 km,  $x$  coordinate 350 ~ 480 km, where overturning and  
 286 breaking of the gravity wave is pronounced.

287 In an alternative hydraulics theory of transition flow, a critical level is still impor-  
 288 tant, but we can find the representations of flows directly, isentropes in the blue box in  
 289 Figure 4 h) exhibit a pattern of initial descent followed by an ascent downstream of the  
 290 convection. This behaviour is consistent with a subcritical flow. A supercritical flow be-  
 291 behaves in the opposite way. In the yellow box, the isentropes exhibit a consistent descent.  
 292 This trend is indicative of transition flow, where the flow undergoes acceleration before  
 293 and after crossing the convection since the state of the flow is converted to supercritical  
 294 flow.

295 In this theory, it is necessary to calculate the Fr to determine the state of the flow.  
 296 It is very complex to calculate this number for this virtual terrain. Though the deep con-  
 297 vection can act as the terrain from previous analysis, it can constantly evolve, and its

298 barrier effects vary at different times and locations, and some air parcels may penetrate  
299 the deep convection directly. Nonetheless, we tentatively separate the jet from the back-  
300 ground by extracting the area from the potential temperature between 338 K and 350 K,  
301 since they envelop the core of the jet and the isentropes, depicting the characteristics of  
302 the transitional flow. By applying the Equation 4, and the  $H$  here can be set as 1500 m  
303 by comparing the same isentropes downstream, we obtain the Fr is 1.08 at 20:10, and  
304 this value indicates a transitional flow can happen. The condition is favourable for downs-  
305 lobe windstorms and a hydraulic jump.

## 306 4 Conclusions

307 In this study, we used the MPAS that utilizes a regionally convection-permitting  
308 mesh to simulate a severe aviation turbulence incident near the Hawaiian Islands. This  
309 model is capable of accurately simulating both the large-scale and local wind fields. Ad-  
310 ditionally, we applied a recently developed subfilter-scale reconstruction method to es-  
311 timate EDR from the convection-permitting model output. Our findings confirm this ap-  
312 proach is effective in predicting aviation turbulence.

313 In this case, the airplane experienced severe turbulence abruptly in the cloud-free  
314 region without any alerts. The environment has convection mostly at lower altitudes,  
315 with very few convective cells occurring above 8000 m. As the airplane typically cruises  
316 at around 12,000 m, relying solely on cloud distribution for warning would assume a smooth  
317 flight process. However, in this case, we find that the turbulence originated from the in-  
318 teraction between the large-scale jet and local deep convection, causing the turbulence  
319 to develop extensively and strongly outside the clouds.

320 The weather conditions of this case created a situation similar to downslope wind-  
321 storms caused by terrain. Deep convection played the role of ‘terrain’ in the air, and the  
322 movement of the turbulent area following the convective system confirmed this effect.  
323 The jet stream, brought to low latitudes by a low-pressure system, has an exit region near  
324 Hawaii. It created the region of a low Scorer parameter immediately above and below  
325 the jet. After passing over the convection, barrier-caused gravity waves broke on the down-  
326 stream side of the convection top and created a wave-induced critical level, which over-  
327 laid with the previously mentioned low Scorer parameter region, amplifying the reflec-  
328 tion of gravity waves and causing the jet to accelerate during its descent. The presence  
329 of continuous descending isentropes during the process and the critical value of the Fr  
330 also suggest the existence of transitional flow. The jet streams created low Richardson  
331 number regions, which favour the generation of severe turbulence. This interaction be-  
332 tween mid-latitude jet streams and deep convection is a new mechanism of aviation tur-  
333 bulence not appreciated before. Our case study provides insights to prevent the encounter  
334 of aviation turbulence in cloud-free regions.

## 335 Open Research Section

336 The ERA5 hourly data in different levels (Bell et al., 2021) can be downloaded on  
337 [https://cds.climate.copernicus.eu/cdsapp#!/dataset/10.24381/cds.bd0915c6](https://cds.climate.copernicus.eu/cdsapp#!/dataset/10.24381/cds.bd0915c6?tab=overview)  
338 [?tab=overview](https://cds.climate.copernicus.eu/cdsapp#!/dataset/10.24381/cds.bd0915c6?tab=overview). The flight data can be downloaded from [https://www.flightradar24](https://www.flightradar24.com/data/flights/ha35)  
339 [.com/data/flights/ha35](https://www.flightradar24.com/data/flights/ha35) (membership required). The GOES-17 (GOES-R Series Pro-  
340 gram, 2019) satellite data can be downloaded from [https://www.av1.class.noaa.gov/](https://www.av1.class.noaa.gov/saa/products/welcome)  
341 [saa/products/welcome](https://www.av1.class.noaa.gov/saa/products/welcome).

## 342 Acknowledgments

343 The project is part of the Aviation Research and Development Project Phase 2 (AvRDP2),  
344 supported by World Meteorological Organization. The authors thank HKUST Fok Ying

345 Tung Research Institute and National Supercomputing Center in Guangzhou Nansha  
346 sub-center for providing high performance computational resources.

## 347 References

- 348 Audrey, C., Christine, L., Yves, B., & Francois, B. (2011, December). Aeronautical  
349 diagnostics for Clear-Air Turbulence forecast at MétéoFrance in the context of  
350 DELICAT European project. *Journal of Physics: Conference Series*, 318(7),  
351 072007. doi: 10.1088/1742-6596/318/7/072007
- 352 Barber, K. A., Mullendore, G. L., & Alexander, M. J. (2018, January). Out-of-  
353 Cloud Convective Turbulence: Estimation Method and Impacts of Model  
354 Resolution. *Journal of Applied Meteorology and Climatology*, 57(1), 121–136.  
355 doi: 10.1175/JAMC-D-17-0174.1
- 356 Bell, B., Hersbach, H., Simmons, A., Berrisford, P., Dahlgren, P., Horányi, A., ...  
357 Thépaut, J.-N. (2021). The ERA5 global reanalysis: Preliminary extension  
358 to 1950. *Quarterly Journal of the Royal Meteorological Society*, 147(741),  
359 4186–4227. doi: 10.1002/qj.4174
- 360 Carruthers, D. J., & Hunt, J. C. R. (1990). Fluid Mechanics of Airflow over Hills:  
361 Turbulence, Fluxes, and Waves in the Boundary Layer. In *Atmospheric Pro-  
362 cesses over Complex Terrain* (pp. 83–107). Boston, MA: American Meteorolog-  
363 ical Society. doi: 10.1007/978-1-935704-25-6\_5
- 364 Chen, F., & Dudhia, J. (2001, April). Coupling an Advanced Land Sur-  
365 face–Hydrology Model with the Penn State–NCAR MM5 Modeling System.  
366 Part I: Model Implementation and Sensitivity. *Monthly Weather Review*,  
367 129(4), 569–585. doi: 10.1175/1520-0493(2001)129<0569:CAALSH>2.0.CO;2
- 368 Chen, H., Liu, H., Leung, C. Y.-Y., Cheung, P., Chan, S. T., & Shi, X. (2023, July).  
369 Predicting convection-induced turbulence with regionally convection-permitting  
370 simulations. *Monthly Weather Review*, Submitted.
- 371 Chow, F. K., Street, R. L., Xue, M., & Ferziger, J. H. (2005, July). Explicit Fil-  
372 tering and Reconstruction Turbulence Modeling for Large-Eddy Simulation of  
373 Neutral Boundary Layer Flow. *Journal of the Atmospheric Sciences*, 62(7),  
374 2058–2077. doi: 10.1175/JAS3456.1
- 375 Clark, T. L., & Peltier, W. R. (1984, November). Critical Level Reflection and the  
376 Resonant Growth of Nonlinear Mountain Waves. *Journal of the Atmospheric  
377 Sciences*, 41(21), 3122–3134. doi: 10.1175/1520-0469(1984)041<3122:CLRATR>  
378 2.0.CO;2
- 379 Doyle, J. D., & Smith, R. B. (2003). Mountain waves over the Hohe Tauern: Influ-  
380 ence of upstream diabatic effects. *Quarterly Journal of the Royal Meteorologi-  
381 cal Society*, 129(588), 799–823. doi: 10.1256/qj.01.205
- 382 Durran, D. (2003). LEE WAVES AND MOUNTAIN WAVES. In *Encyclopedia of  
383 Atmospheric Sciences* (pp. 1161–1169). Elsevier. doi: 10.1016/B0-12-227090-8/  
384 00202-5
- 385 Durran, D. R. (1986, November). Another Look at Downslope Windstorms. Part  
386 I: The Development of Analogs to Supercritical Flow in an Infinitely Deep,  
387 Continuously Stratified Fluid. *Journal of the Atmospheric Sciences*, 43(21),  
388 2527–2543. doi: 10.1175/1520-0469(1986)043<2527:ALADWP>2.0.CO;2
- 389 Ellrod, G. P., & Knapp, D. I. (1992, March). An Objective Clear-Air Turbulence  
390 Forecasting Technique: Verification and Operational Use. *Weather and Fore-  
391 casting*, 7(1), 150–165. doi: 10.1175/1520-0434(1992)007<0150:AOCATF>2.0  
392 .CO;2
- 393 Fudeyasu, H., Kuwagata, T., Ohashi, Y., Suzuki, S.-i., Kiyohara, Y., & Hozumi,  
394 Y. (2008, January). Numerical Study of the Local Downslope Wind  
395 “Hirodo-Kaze” in Japan. *Monthly Weather Review*, 136(1), 27–40. doi:  
396 10.1175/2007MWR2049.1
- 397 Fujita, T. T. (1982). Principle of Stereoscopic Height Computations and their Appli-

- 398           cations to Stratospheric Cirrus over Severe Thunderstorms. *Journal of the Me-*  
399 *teorological Society of Japan. Ser. II, 60(1)*, 355–368. doi: 10.2151/jmsj1965.60  
400 .1.355
- 401 GOES-R Series Program. (2019). *NOAA GOES-R Series Advanced Baseline Imager*  
402 *(ABI) Level 0 Data*. NOAA National Centers for Environmental Information.  
403 doi: 10.25921/TVWS-W071
- 404 Hong, S.-Y. (2010, July). A new stable boundary-layer mixing scheme and its im-  
405 pact on the simulated East Asian summer monsoon. *Quarterly Journal of the*  
406 *Royal Meteorological Society, 136(651)*, 1481–1496. doi: 10.1002/qj.665
- 407 Hong, S.-Y., Kim, J.-h., Lim, J.-o., & Dudhia, J. (2006, March). The WRF sin-  
408 gle moment microphysics scheme (WSM). *Journal of the Korean Meteorological*  
409 *Society, 42*, 129–151.
- 410 Iacono, M. J., Mlawer, E. J., Clough, S. A., & Morcrette, J.-J. (2000, June). Impact  
411 of an improved longwave radiation model, RRTM, on the energy budget and  
412 thermodynamic properties of the NCAR community climate model, CCM3.  
413 *Journal of Geophysical Research: Atmospheres, 105(D11)*, 14873–14890. doi:  
414 10.1029/2000JD900091
- 415 Kim, S.-H., & Chun, H.-Y. (2016, October). Aviation turbulence encounters de-  
416 tected from aircraft observations: Spatiotemporal characteristics and applica-  
417 tion to Korean Aviation Turbulence Guidance: Aviation turbulence encounters  
418 detected from aircraft observations. *Meteorological Applications, 23(4)*, 594–  
419 604. doi: 10.1002/met.1581
- 420 Klemp, J. B., & Lilly, D. R. (1975, February). The Dynamics of Wave-Induced  
421 Downslope Winds. *Journal of the Atmospheric Sciences, 32(2)*, 320–339. doi:  
422 10.1175/1520-0469(1975)032<0320:TADOWID>2.0.CO;2
- 423 Koletsis, I., Lagouvardos, K., Kotroni, V., & Bartzokas, A. (2009, October). Numer-  
424 ical study of a downslope windstorm in Northwestern Greece. *Atmospheric Re-*  
425 *search, 94(2)*, 178–193. doi: 10.1016/j.atmosres.2009.05.012
- 426 Lane, T. P., Sharman, R. D., Clark, T. L., & Hsu, H.-M. (2003, May). An Investi-  
427 gation of Turbulence Generation Mechanisms above Deep Convection. *Journal*  
428 *of the Atmospheric Sciences, 60(10)*, 1297–1321. doi: 10.1175/1520-0469(2003)  
429 60<1297:AOTGM>2.0.CO;2
- 430 Long, R. R. (1953, February). Some Aspects of the Flow of Stratified Fluids: I. A  
431 Theoretical Investigation. *Tellus, 5(1)*, 42–58. doi: 10.1111/j.2153-3490.1953  
432 .tb01035.x
- 433 Mlawer, E. J., Taubman, S. J., Brown, P. D., Iacono, M. J., & Clough, S. A. (1997,  
434 July). Radiative transfer for inhomogeneous atmospheres: RRTM, a validated  
435 correlated-k model for the longwave. *Journal of Geophysical Research: Atmo-*  
436 *spheres, 102(D14)*, 16663–16682. doi: 10.1029/97JD00237
- 437 Nakanishi, M., & Niino, H. (2009). Development of an Improved Turbulence Closure  
438 Model for the Atmospheric Boundary Layer. *Journal of the Meteorological So-*  
439 *ciety of Japan. Ser. II, 87(5)*, 895–912. doi: 10.2151/jmsj.87.895
- 440 O’Neill, M. E., Orf, L., Heymsfield, G. M., & Halbert, K. (2021, September). Hy-  
441 draulic jump dynamics above supercell thunderstorms. *Science (New York,*  
442 *N. Y.), 373(6560)*, 1248–1251. doi: 10.1126/science.abh3857
- 443 Oxenden, M. (2023, January). Cloud ‘Shot Up’ Just Before Severe Turbulence  
444 Struck, Report Says. *The New York Times*.
- 445 Peltier, W. R., & Clark, T. L. (1979, August). The Evolution and Stability of  
446 Finite-Amplitude Mountain Waves. Part II: Surface Wave Drag and Severe  
447 Downslope Windstorms. *Journal of the Atmospheric Sciences, 36(8)*, 1498–  
448 1529. doi: 10.1175/1520-0469(1979)036<1498:TEASOF>2.0.CO;2
- 449 Prósper, M. A., Sosa Tinoco, I., Otero-Casal, C., & Miguez-Macho, G. (2019, July).  
450 Downslope windstorms in the Isthmus of Tehuantepec during Tehuantepecer  
451 events: A numerical study with WRF high-resolution simulations. *Earth*  
452 *System Dynamics, 10(3)*, 485–499. doi: 10.5194/esd-10-485-2019

- 453 Schumann, U. (1991, August). Subgrid length-scales for large-eddy simulation of  
 454 stratified turbulence. *Theoretical and Computational Fluid Dynamics*, 2(5),  
 455 279–290. doi: 10.1007/BF00271468
- 456 Sharman, R., & Lane, T. (Eds.). (2016a). *Aviation Turbulence*. Cham: Springer In-  
 457 ternational Publishing. doi: 10.1007/978-3-319-23630-8
- 458 Sharman, R., & Lane, T. (Eds.). (2016b). *Aviation Turbulence*. Cham: Springer In-  
 459 ternational Publishing. doi: 10.1007/978-3-319-23630-8
- 460 Sharman, R. D., Doyle, J. D., & Shapiro, M. A. (2012, January). An Investigation  
 461 of a Commercial Aircraft Encounter with Severe Clear-Air Turbulence over  
 462 Western Greenland. *Journal of Applied Meteorology and Climatology*, 51(1),  
 463 42–53. doi: 10.1175/JAMC-D-11-044.1
- 464 Sharman, R. D., Trier, S. B., Lane, T. P., & Doyle, J. D. (2012, June). Sources  
 465 and dynamics of turbulence in the upper troposphere and lower stratosphere:  
 466 A review: FRONTIER. *Geophysical Research Letters*, 39(12), n/a-n/a. doi:  
 467 10.1029/2012GL051996
- 468 Skamarock, W. C., Klemp, J. B., Duda, M. G., Fowler, L. D., Park, S.-H., &  
 469 Ringler, T. D. (2012, September). A Multiscale Nonhydrostatic Atmospheric  
 470 Model Using Centroidal Voronoi Tessellations and C-Grid Staggering. *Monthly*  
 471 *Weather Review*, 140(9), 3090–3105. doi: 10.1175/MWR-D-11-00215.1
- 472 Smith, R. B. (1985, December). On Severe Downslope Winds. *Journal of the Atmo-*  
 473 *spheric Sciences*, 42(23), 2597–2603. doi: 10.1175/1520-0469(1985)042<2597:  
 474 OSDW>2.0.CO;2
- 475 Smolarkiewicz, P. K., & Rotunno, R. (1989, April). Low Froude Number Flow  
 476 Past Three-Dimensional Obstacles. Part I: Baroclinically Generated Lee  
 477 Vortices. *Journal of the Atmospheric Sciences*, 46(8), 1154–1164. doi:  
 478 10.1175/1520-0469(1989)046<1154:LFNFPT>2.0.CO;2
- 479 Thompson, G., Field, P. R., Rasmussen, R. M., & Hall, W. D. (2008, December).  
 480 Explicit Forecasts of Winter Precipitation Using an Improved Bulk Micro-  
 481 physics Scheme. Part II: Implementation of a New Snow Parameterization.  
 482 *Monthly Weather Review*, 136(12), 5095–5115. doi: 10.1175/2008MWR2387.1
- 483 Trier, S. B., Sharman, R. D., & Lane, T. P. (2012, August). Influences of Moist Con-  
 484 vection on a Cold-Season Outbreak of Clear-Air Turbulence (CAT). *Monthly*  
 485 *Weather Review*, 140(8), 2477–2496. doi: 10.1175/MWR-D-11-00353.1
- 486 Tvaryanas, A. P. (2003, September). Epidemiology of Turbulence-Related Injuries in  
 487 Airline Cabin Crew, 1992–2001. *Aviation, Space, and Environmental Medicine*,  
 488 74(9), 970–976.

Figure 1.

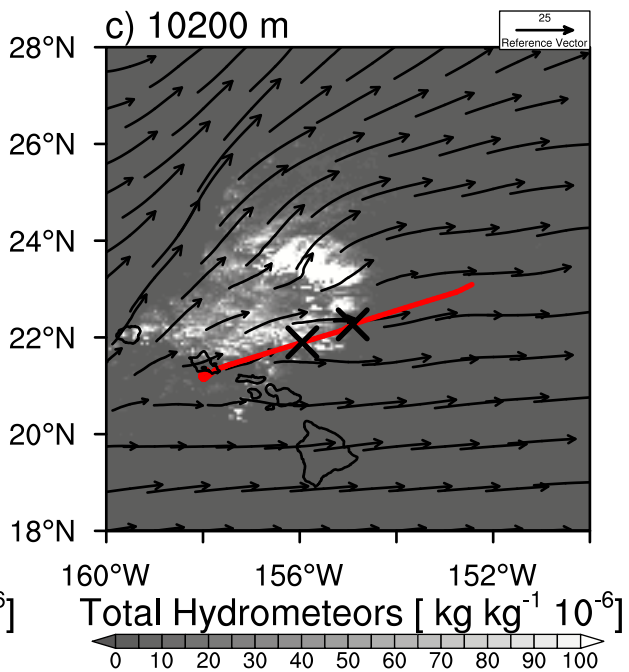
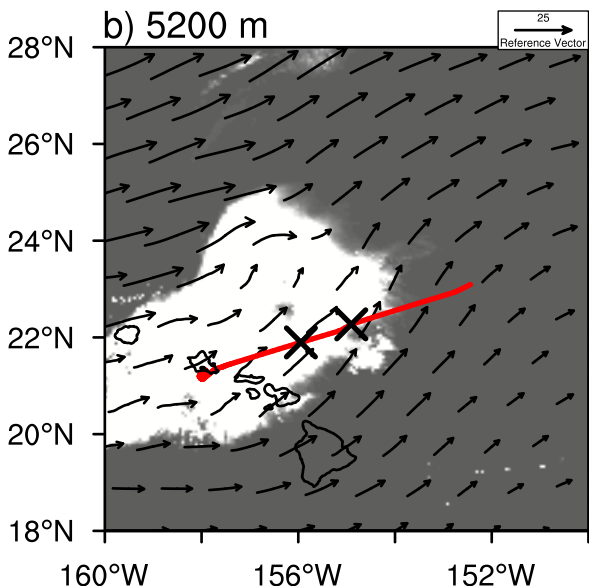
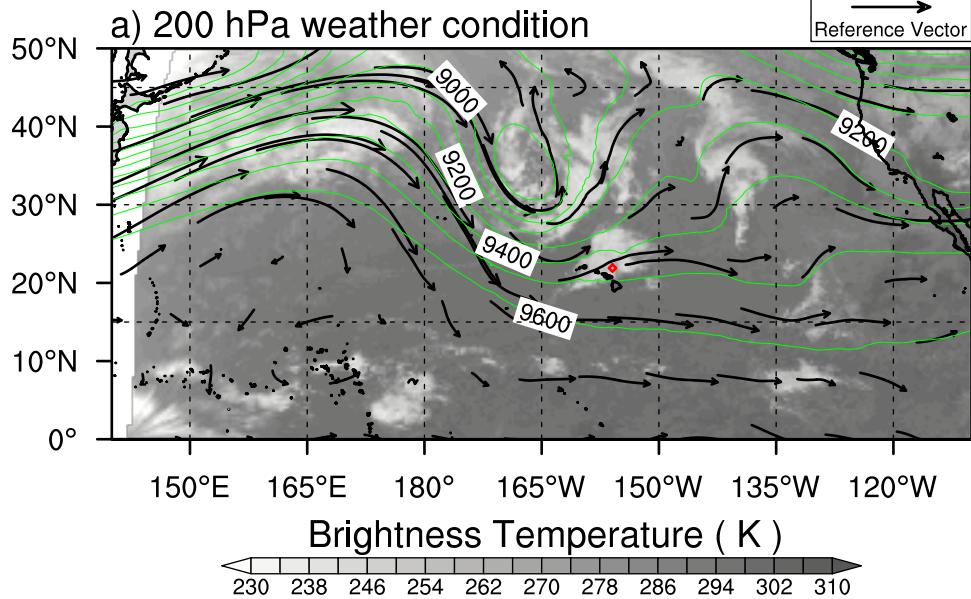


Figure 2.

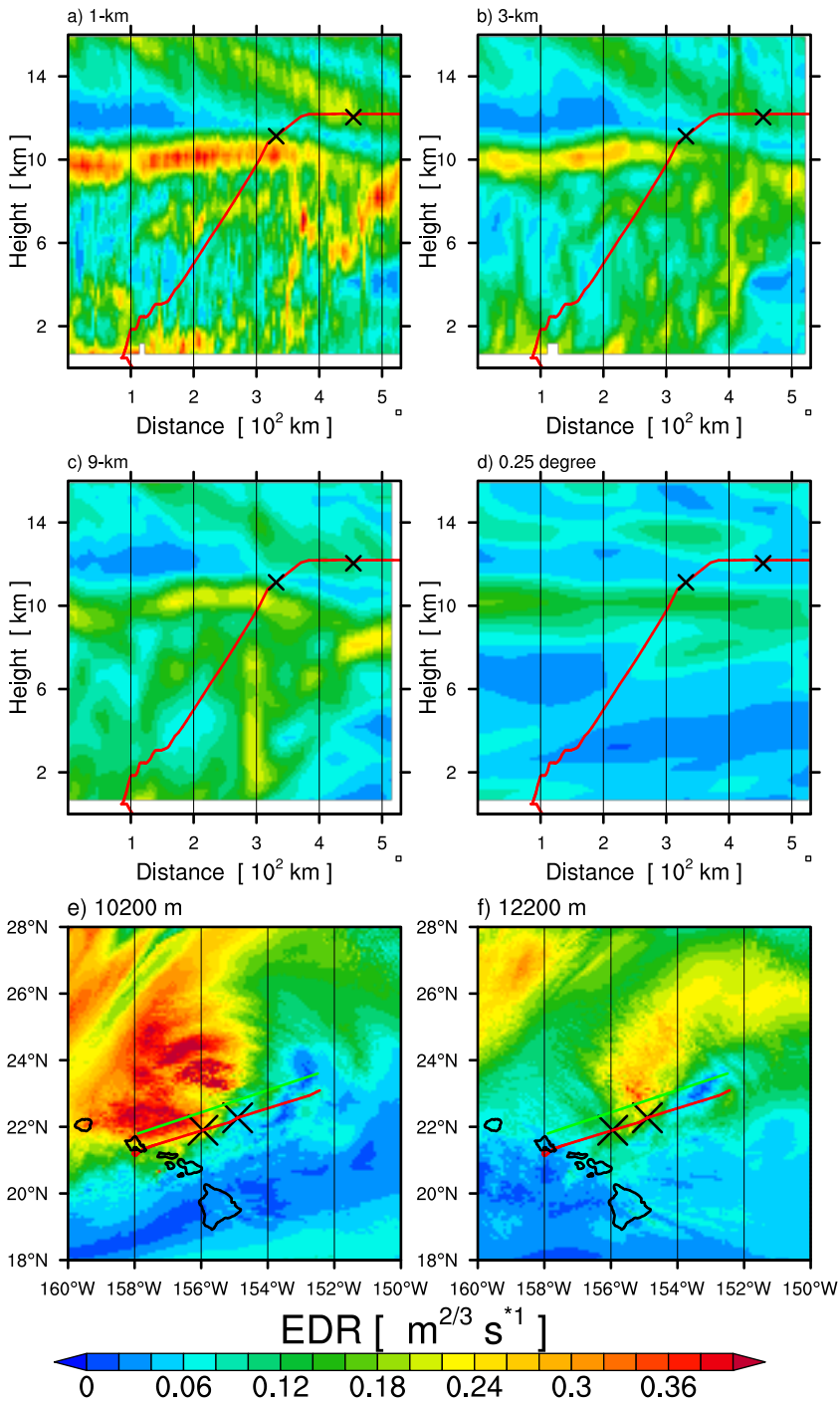


Figure 3.

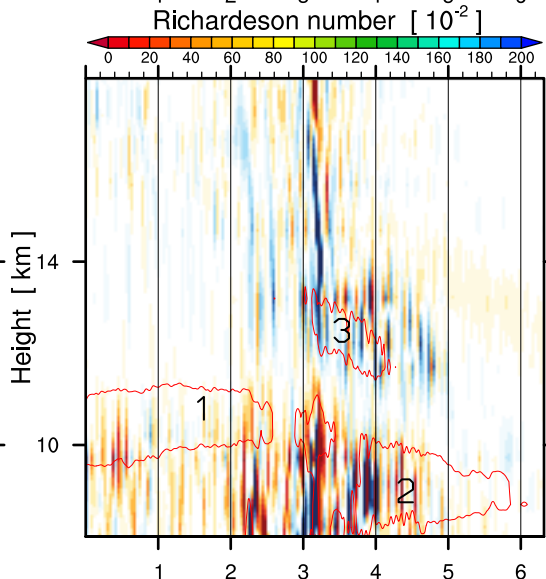
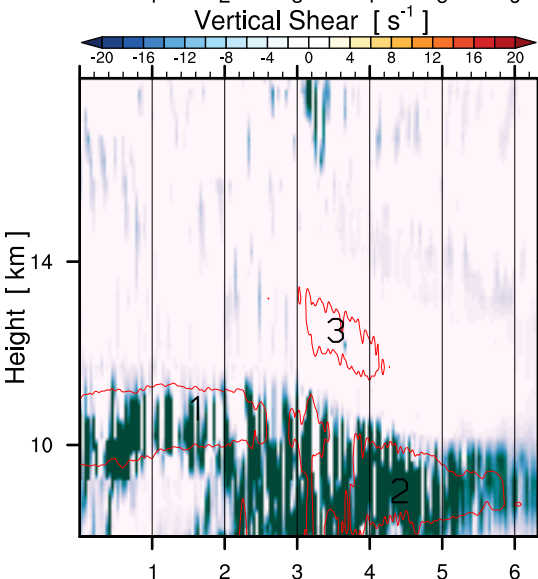
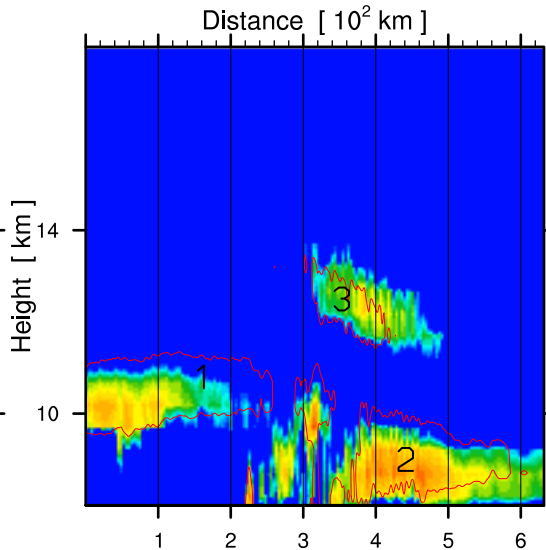
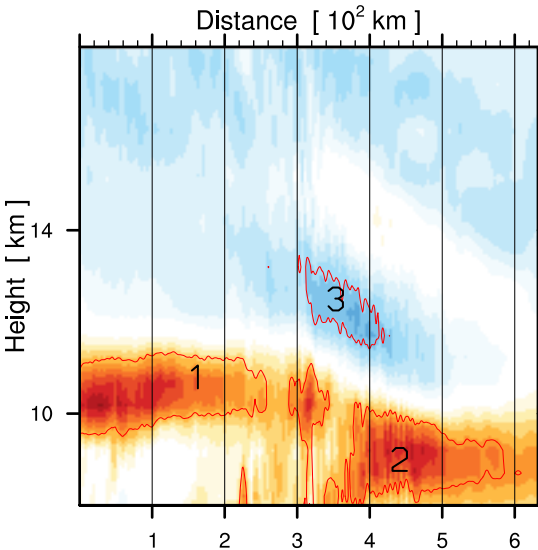
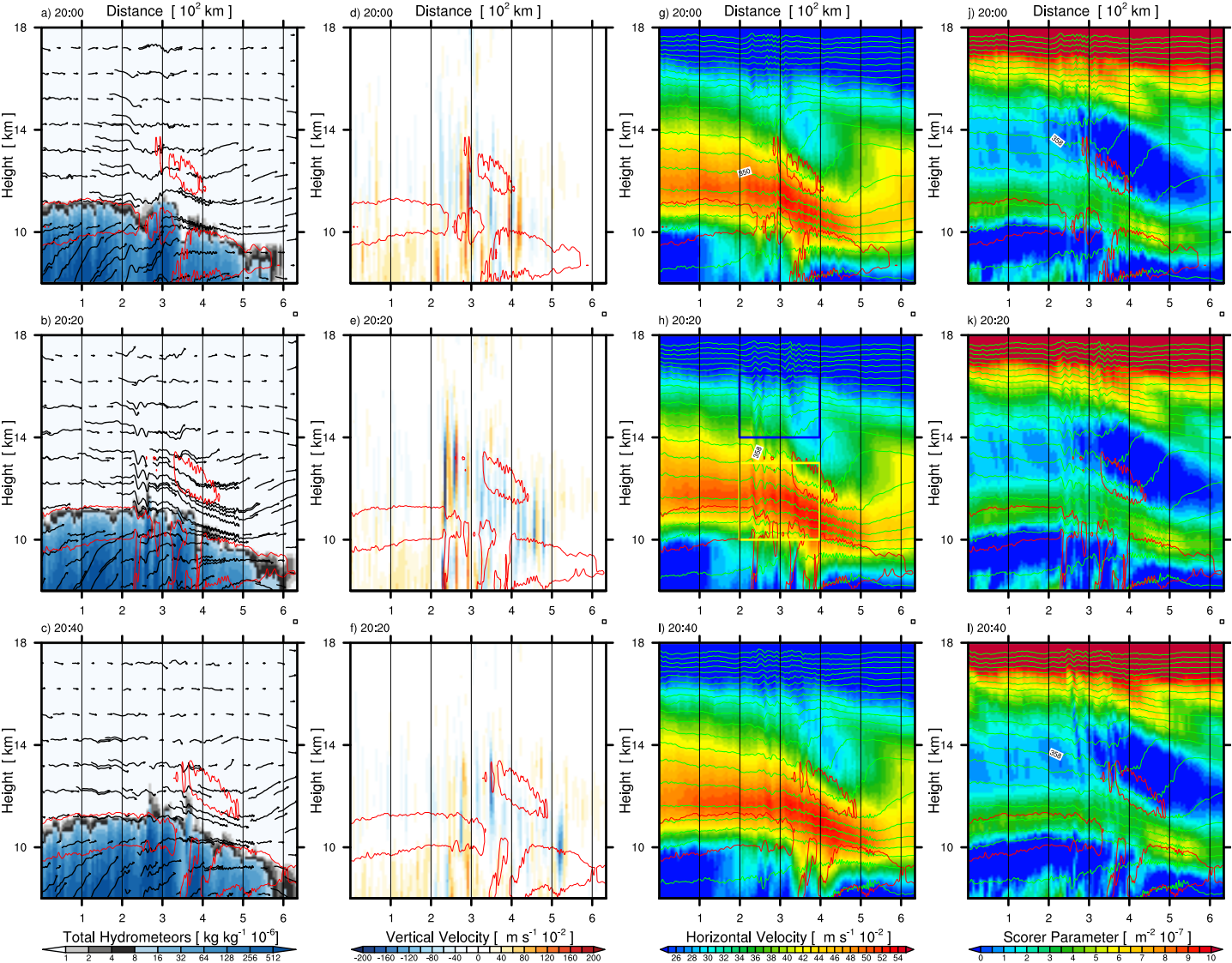


Figure 4.



# Aviation Turbulence Induced by the Interaction between a Jet Stream and Deep Convection

Haoming Chen<sup>1</sup>, Xiaoming Shi<sup>1</sup>, Christy Yan Yu Leung<sup>2</sup>, Ping Cheung<sup>2</sup>, Pak

Wai Chan<sup>2</sup>

<sup>1</sup>Division of Environment and Sustainability, Hong Kong University of Science and Technology, Hong Kong, China

<sup>2</sup>Hong Kong Observatory, Hong Kong, China

## Contents of this file

1. Figure S1
2. Figure S2
3. Figure S3

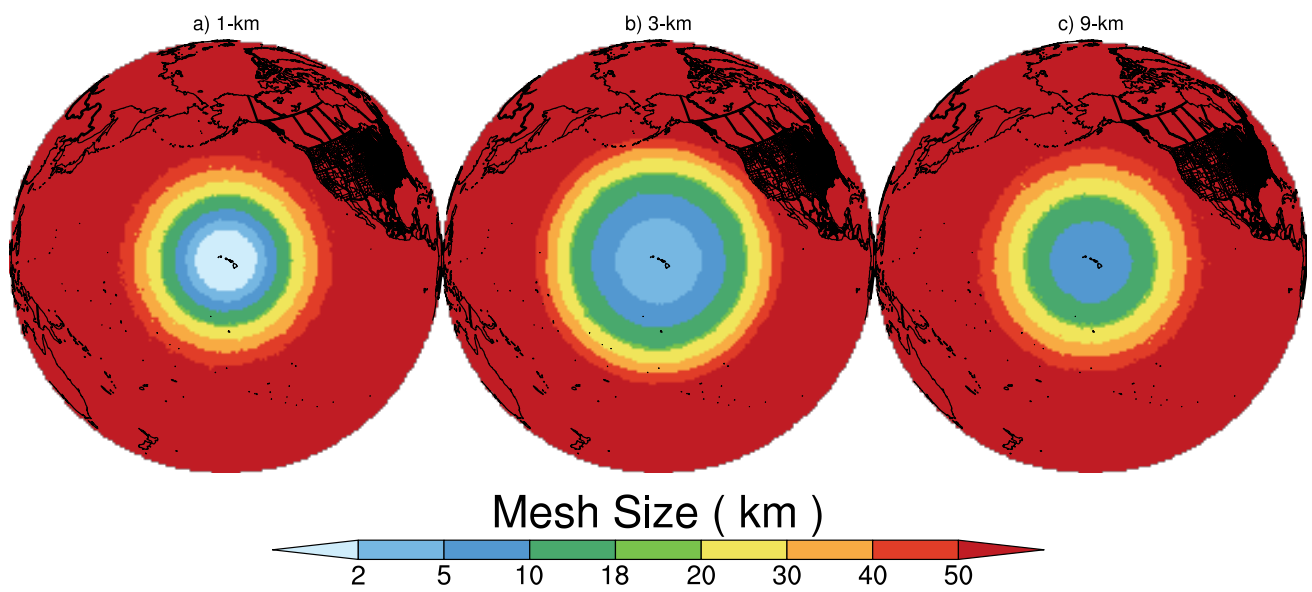


**Figure S1.** Global variable-resolution mesh size distribution in the variable-resolution a) 1 ~ 60 km, b) 3 ~ 60 km and c) 9 ~ 60 km experiments.

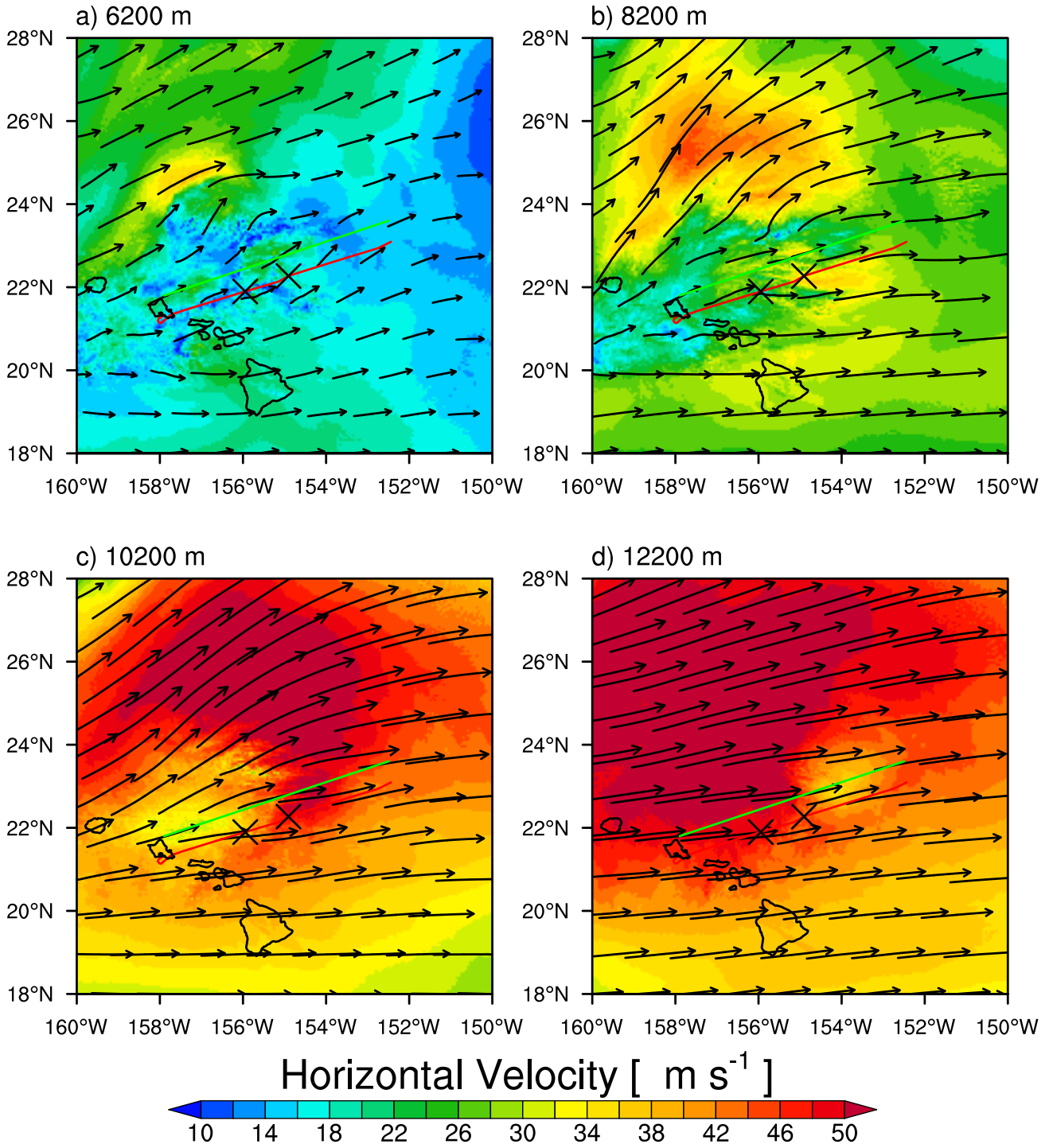


**Figure S2.** Horizontal distribution of the wind speed at at December 18, 2022, 20:10 UTC from different levels a) 6200 m, b) 9200 m, c) 10200 m and d) 12200 m. The red line represents the path of the airplane, the two notations represent the positions of possible turbulence events.

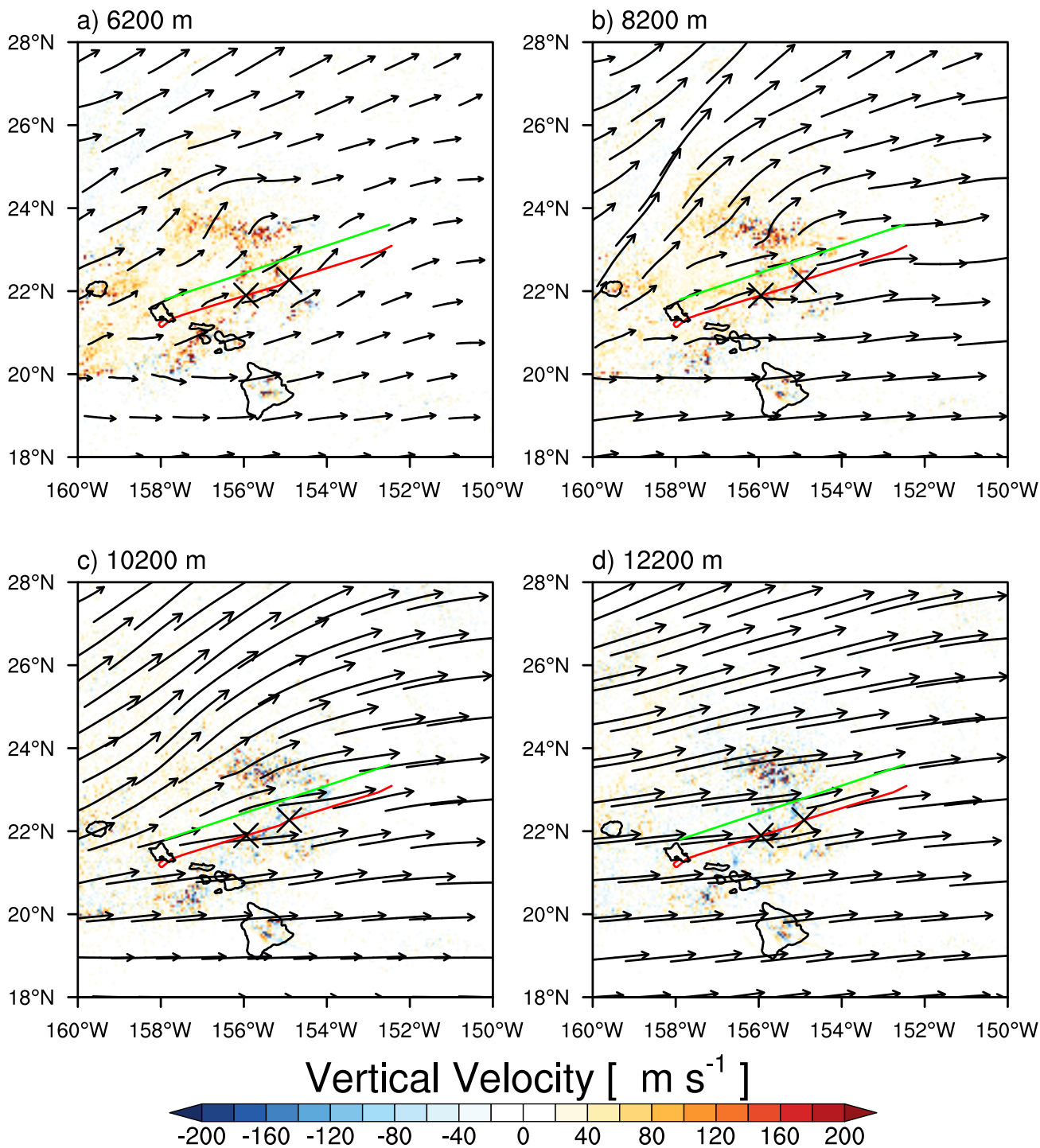


**Figure S3.** Vertical distribution of the wind speed at at December 18, 2022, 20:10 UTC from different levels a) 6200 m , b) 9200 m , c) 10200 m and d) 12200 m . The red line r represents the path of the airplane, the two notations represent the positions of possible turbulence events.